Chemical Science

ROYAL SOCIETY OF CHEMISTRY

EDGE ARTICLE

View Article Online
View Journal | View Issue

Cite this: *Chem. Sci.*, 2021, **12**, 5918

All publication charges for this article have been paid for by the Royal Society of Chemistry

Rational design of iridium–porphyrin conjugates for novel synergistic photodynamic and photothermal therapy anticancer agents†

Liping Zhang,‡[a] Yun Geng,‡[a] Lijuan Li,[a] Xiaofan Tong,[a] Shi Liu,[b] Xingman Liu,[a] Zhongmin Su,[a] Zhigang Xie,*[b] Dongxia Zhu*[a] and Martin R. Bryce*[c]

Near-infrared (NIR) emitters are important probes for biomedical applications. Nanoparticles (NPs) incorporating mono- and tetranuclear iridium(III) complexes attached to a porphyrin core have been synthesized. They possess deep-red absorbance, long-wavelength excitation (635 nm) and NIR emission (720 nm). TD-DFT calculations demonstrate that the iridium–porphyrin conjugates herein combine the respective advantages of small organic molecules and transition metal complexes as photosensitizers (PSs): (i) the conjugates retain the long-wavelength excitation and NIR emission of porphyrin itself; (ii) the conjugates possess highly effective intersystem crossing (ISC) to obtain a considerably more long-lived triplet photoexcited state. These photoexcited states do not have the usual radiative behavior of phosphorescent Ir(III) complexes, and they play a very important role in promoting the singlet oxygen ($^1O_2$) and heat generation required for photodynamic therapy (PDT) and photothermal therapy (PTT). The tetranuclear **4-Ir** NPs exhibit high $^1O_2$ generation ability, outstanding photothermal conversion efficiency (49.5%), good biocompatibility, low half-maximal inhibitory concentration (IC_{50}) (0.057 μM), excellent photothermal imaging and synergistic PDT and PTT under 635 nm laser irradiation. To our knowledge this is the first example of iridium–porphyrin conjugates as PSs for photothermal imaging-guided synergistic PDT and PTT treatment *in vivo*.

Received 8th January 2021
Accepted 22nd March 2021

DOI: 10.1039/d1sc00126d

rsc.li/chemical-science

Introduction

Transition metal complexes have made remarkable achievements in the clinical treatment of neuropathy, tumor therapy and diabetes.[1] Phosphorescent iridium(III) complexes are especially attracting attention as photosensitizers (PSs) for phototherapy, owing to the excellent photothermal stability and high intersystem crossing (ISC) ability.[2–8] Unfortunately, the currently reported PSs based on Ir(III) complexes are far from ideal, and suffer from some obvious drawbacks: (1) the inherent short excitation wavelength (*ca.* 450 nm) leads to autofluorescence interference, poor tissue penetration and a lack of selective uptake by neoplastic tissue;[9–13] (2) their applications have mainly focused on photodynamic therapy (PDT), and consequently their therapeutic effect is highly subject to the oxygen content in the tumor, and tumor hypoxia limits the formation of reactive oxygen species (ROS) which ultimately leads to cancer cell death;[14,15] (3) there are very few reports on their application in photothermal therapy (PTT), which seriously limits their applications in phototherapy.[16–18] Therefore, there is an urgent need to design Ir(III) complexes as PSs that can overcome the above shortcomings and can achieve more optimal tumor therapies.

PSs with long-wavelength excitation and deeper tissue penetration are crucial to guarantee effective clinical applications.[19,20] Studies have sought to extend the phototherapeutic window by introducing fluorescent groups into Ir(III) complexes, such as boron dipyrromethene (BODIPY)[21] and coumarin.[22,23] This strategy merges the advantages of Ir(III) complexes with long-lived triplet metal–ligand charge transfer (^{3}MLCT) states and fluorescent molecular π–π* transitions, leading to promising anticancer activity.[12] Most of these reported PSs require excitation with short-wavelength light, which is ineffective for deep tumors.[3,4,24] PTT is usually triggered by red light and the absorbed light energy can be converted into heat, which provides a thermal effect leading to the apoptosis of cancer cells.[25–29] More importantly, PTT is independent of the oxygen concentration, and is thus an excellent candidate to treat

[a]*Key Laboratory of Nanobiosensing and Nanobioanalysis at Universities of Jilin Province, Department of Chemistry, Northeast Normal University, 5268 Renmin Street, Changchun, Jilin Province 130024, P. R. China. E-mail: zhudx047@nenu.edu.cn*

[b]*State Key Laboratory of Polymer Physics and Chemistry, Changchun Institute of Applied Chemistry, Chinese Academy of Sciences, Changchun, 130022, P. R. China. E-mail: xiez@ciac.ac.cn*

[c]*Department of Chemistry, Durham University, Durham, DH1 3LE, UK. E-mail: m.r.bryce@durham.ac.uk*

† Electronic supplementary information (ESI) available. See DOI: 10.1039/d1sc00126d

‡ These authors contributed equally to this work.

hypoxic tumors, which will effectively make up for the deficiency of PDT. However, few research works have studied Ir(III) complexes as PSs for PTT, which is likely due to their short excitation wavelength (*ca.* 450 nm) caused by the typical ^{3}MLCT process. Additionally, the photothermal effect is beneficial to promote the internalization of PSs and oxygen in the tumor tissues, thereby further improving the PDT effect.[30–33] Hence, synergistic PDT and PTT treatment is a more effective prospect for tumor therapy in terms of concurrent metastasis than single PDT or PTT.[34–40] Therefore, achieving long-wavelength excitation of PSs is a very important goal to realize PTT and to effectively overcome the oxygen dependence in PDT, and ultimately to improve the clinical outcome of phototherapy.

Porphyrin derivatives have been utilized as phototherapy reagents due to their absorption in the red-light region, although this absorption is of relatively low intensity.[41] Specific varied examples include tetraphenylchlorin as a photosensitizer, a phosphatidylcholine-pyropheophorbide conjugate, a diphenylporphyrin conjugated polymer and a chlorin-based porous organic polymer.[42–46] However, they possess the common drawbacks of the small organic molecular PSs, such as larger energy gap (ΔE_{ST}) between the first singlet excited state (S_1) and triplet state (T_1) and less triplet photoexcited state compared with transition metal complexes, which directly leads to reduced $^1O_2$ production and low photothermal conversion efficiency.[46–50] We asked the following question: Is it possible to combine the respective advantages of small organic molecules and transition metal complex PSs to obtain Ir(III)-porphyrin conjugates with long-wavelength excitation for high-efficiency synergistic PDT and PTT treatment?

We recently reported that multinuclear Ir(III) complexes encapsulated in nanoparticles (NPs) have good biocompatibility, and that they can increase ^{3}MLCT transitions and molar absorption coefficients, resulting in excellent PDT effects.[51] However, their short excitation wavelength (450 nm) is unsatisfactory for *in vivo* treatment due to poor tissue penetration. We hypothesized that combining the advantages of long-wavelength excitation and NIR emission of porphyrin itself, and highly effective long-lived triplet photoexcited state of transition metal complexes, inhibiting the phosphorescent emission from transition metal complexes simultaneously, would be a good strategy to enhance the photosensitizer-assisted (PS-assisted) phototherapy, PDT and PTT.

Results and discussion

Recent promising metal–porphyrin conjugates include: porphyrinoid-Pt(II) conjugates;[52] metal–organic frameworks with porphyrin ligands;[53] a porphyrin–Ru complex conjugate;[54] and a combination of cationic Cu–porphyrin with Schiff base Cu complexes.[55] These covalent porphyrin-transition metal conjugates, used for PDT only, are structurally very different from the molecules reported herein for PDT and PTT. In this work, we synthesized two porphyrin derivatives substituted with mono- and tetra-Ir(III) complexes, named **1-Ir** and **4-Ir**, respectively (Fig. 1A), both of which can be excited with long-wavelength light, and their corresponding polymer-encapsulated NPs, named **1-Ir** NPs and **4-Ir** NPs. The iridium complexes have a stereogenic metal center and will exist as a mixture of Λ and Δ enantiomers. Separation of the enantiomers of an Ir complex is rarely accomplished and is beyond the scope of the present work.[56] Tetraphenylporphyrin (**TPP**), a standard PS,[42–46] is studied as a comparison to **1-Ir** and **4-Ir**. The detailed synthetic procedures and spectroscopic characterization of **TPP**, **1-Ir** and **4-Ir** are reported in the ESI (Fig. S1–S13†). The **4-Ir** molecule has a smaller ΔE_{ST} and stronger spin–orbit couplings compared with **TPP** and **1-Ir**, thereby significantly promoting the generation of abundant and effective triplet photoexcited state through intersystem crossing. **4-Ir** NPs possess deep-red absorption, long-wavelength excitation (635 nm), near-infrared (NIR) emission, high $^1O_2$ generation ability, outstanding photothermal conversion efficiency (49.5%) and good biocompatibility. More importantly, the temperature of tumors injected with **4-Ir** NPs could reach to 61.9 °C after laser irradiation, and good photothermal imaging has been accomplished. The synergistic PDT and PTT effect of **4-Ir** NPs gives high-efficiency inhibition of tumor growth *in vivo*.

To study the molecular properties of **TPP**, **L4**, **1-Ir**, and **4-Ir**, density functional theory (DFT) and time-dependent (TD-DFT) calculations were performed in Gaussian 16. As shown in Fig. S14,† the HOMO and LUMO of **TPP** and **L4** with a large overlap are delocalized on the π-conjugated porphyrin ring. On the contrary, **1-Ir** and **4-Ir** exhibit obvious HOMO–LUMO separation. The HOMO–LUMO energy gap decreases with the increasing number of Ir centers from **TPP** (2.72 eV) to **4-Ir** (2.31 eV). The calculations show that both the HOMO and LUMO energy levels of **L4** are raised somewhat compared to **TPP** (Fig. S14†). However, the energy gap of **L4** (2.63 eV) is changed little compared with **TPP** (2.72 eV) and its energy gap is still significantly larger than that of **Ir-4** (2.26 eV) (Fig. S14†). The relatively narrow gap suggests a long-wavelength absorption, especially for **4-Ir**, which is promising for phototherapy. The attached Ir complexes filled the missing excited states of the porphyrin and did not affect the distribution of the excited states of the porphyrin itself (Fig. 1B). As shown in Fig. 1C, the strong absorptions in the long-wavelength region corresponding to singlet excited states S_5 and S_9, which are close to the absorptions of **TPP**, are derived from contributions of the porphyrin unit. The lowest triplet excited state (T_1) was mainly contributed by the local charge-transfer transition in the ligands (^{3}LC) of one cyclometalated Ir complex. The absence of orbital participation from the Ir atoms indicates that there is no phosphorescent emission in **4-Ir**. This means that **4-Ir** complex still retains long-wavelength excitation and near-infrared emission originating from porphyrin, while a more long-lived triplet photoexcited state is generated from the cyclometalated Ir(III) fragments. Thereby, the participation of the cyclometalated Ir(III) complexes at the singlet (S_n) and triplet (T_n) excited states is beneficial to the inter-system crossing (ISC) of **4-Ir**. The energy gap between S_1 and T_1 is reduced from **TPP** (0.79 eV) to **4-Ir** (0.56 eV) as shown in Fig. 1B. At the same time, the singlet and triplet photoexcited state with close energy levels also increased along with the additional number of Ir centers (Fig. 1B). The emission and transient decay of **4-Ir** are shown in

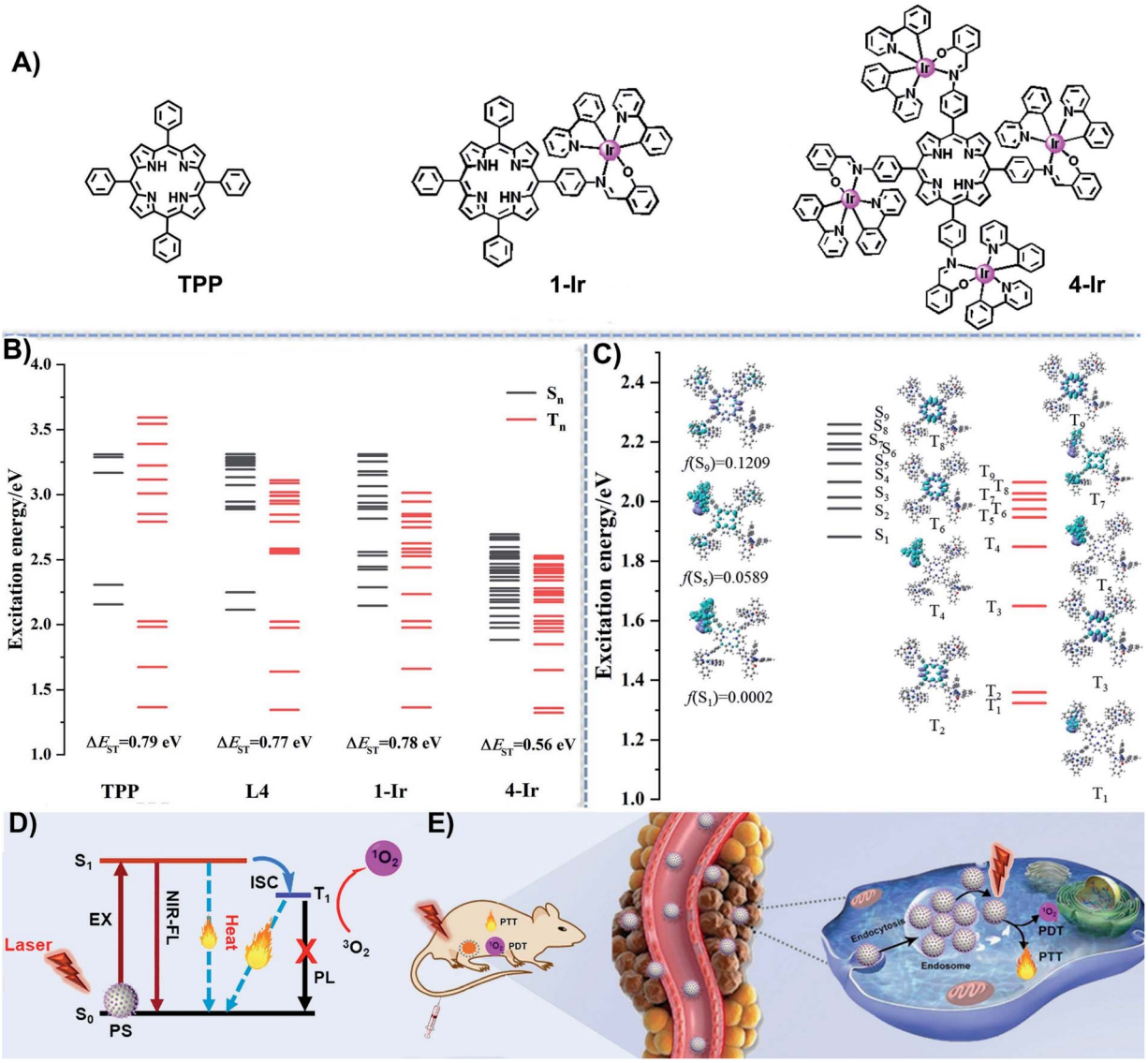

Fig. 1 (A) Chemical structures of TPP, 1-Ir and 4-Ir; (B) the calculated excitation energy distributions of singlet (S_n) and triplet (T_n) excited states for TPP, L4, 1-Ir and 4-Ir; (C) the transition charge density differences (CDD) for singlet (S_n) and triplet (T_n) excited states in 4-Ir; (D) the photophysical mechanism for photoactive cancer therapy using PSs; (E) schematic illustration of PSs for *in vivo* photophysical applications.

Fig. S22.† The short excited-state lifetime (τ 4.76 ns) indicates that the fluorescence of **4-Ir** is from the porphyrin unit and not from the attached Ir complexes.

Due to the large molecular size of **4-Ir**, we take the spin–orbit coupling values of **TPP** and **1-Ir** as examples to find the contribution of the attached Ir complexes in increasing the ISC ability. Compared with **TPP**, the spin–orbit coupling constants between S_n and T_n of **1-Ir** complex increased considerably from 0.297 to 148 cm^{-1}, as shown in Table S1.† These data indicate that the spin–orbit coupling values in **4-Ir** should be enhanced to an even greater extent. Meanwhile, a comparison of the geometrical structures at S_0 and T_1 states for **TPP** and **4-Ir**, together with their respective root mean square deviation (RMSD) (0.16 Å and 0.46 Å) suggests a larger nonradiative vibrational relaxation of **4-Ir**, as shown in Fig. S16.† The results indicate that the attached cyclometalated Ir complexes without phosphorescent emission play very important roles in: (i) greatly improving the highly effective ISC ability to ensure sufficient triplet photoexcited states; (ii) greatly promoting the nonradiative vibrational processes for the energy conversion. Therefore, theoretical results support our proposed design concept: namely, to realize an advantageous combination of the photophysical performance of porphyrin and iridium complexes.

The **TPP** NPs, **1-Ir** NPs and **4-Ir** NPs were prepared by polymer-encapsulation (Fig. 2A).[57–62] The introduced amphiphilic polymer chain (DSPE-PEG-MAL) was used to obviously change the biocompatibility of the compound.[51,57] HIV-1 Tat as the cell penetrating peptide can effectively promote the entry of NPs into cells.[51,57] Transmission electron microscopy (TEM) images confirmed that **TPP** NPs, **1-Ir** NPs and **4-Ir** NPs exhibit spherical morphologies with average diameters of about 44, 48, 57 nm, respectively (Fig. 2B). Similar features were observed in

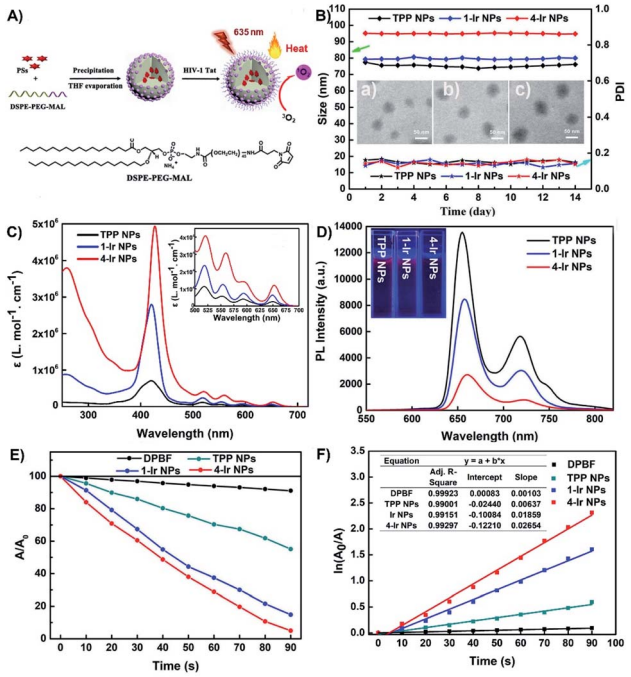

Fig. 2 (A) The synthesis of NPs; (B) stability of size distribution of different PSs during 14 days, inset: the TEM images of (a) **TPP** NPs, (b) **1-Ir** NPs and (c) **4-Ir** NPs; (C), (D) UV-vis absorption and emission spectra of PSs in water (1×10^{-5} M) inset: emission images of the PSs under 365 nm UV illumination; (E) the decomposition rates of DPBF (1.5×10^{-5} M) with different PSs (1×10^{-6} M) under irradiation (635 nm, 0.4 W cm^{-2}); (F) time-dependent kinetics of $^1O_2$ generation. A_0 = absorption of DPBF without irradiation. A = real-time absorption of DPBF with different irradiation times.

the scanning electron microscopy (SEM) images (Fig. S17†). The hydrodynamic diameters of **TPP** NPs, **1-Ir** NPs and **4-Ir** NPs determined by dynamic light scattering (DLS) are 74, 79 and 95 nm, respectively (Fig. S18; Table S3†). The larger sizes measured by DLS than by TEM can be attributed to a hydrated layer on the NPs. In addition, the zeta potential of the **4-Ir** NPs was determined to be +27.8 mV, confirming that HIV-1 Tat was successfully conjugated to the surface of NPs.[61,62] **4-Ir** NPs released a low amount of **4-Ir** (≈1.69%) over 72 h in water (Fig. S19†). Such a low release of contents verifies that the PSs remain intact as the active species. Moreover, no obvious changes of the size or size distribution of **TPP** NPs, **1-Ir** NPs and **4-Ir** NPs were observed within 14 days suggesting the high stability of the NPs. In addition, the size of **4-Ir** NPs in serum (118 nm) and PBS (106 nm) is stable within 14 days (Fig. S24†). These NPs with spherical morphology, appropriate size and excellent stability are suited for biological applications.

The UV-vis absorption and photoluminescence (PL) spectra of **TPP** NPs, **1-Ir** NPs and **4-Ir** NPs were recorded in water. The extended absorption band in the 500–700 nm region (Fig. 2C) is advantageous for matching long-wavelength excitation to enhance tissue penetration. The UV-Vis absorption spectra of the corresponding pure compounds, **TPP**, **1-Ir** and **4-Ir**, exhibit similar absorption bands in tetrahydrofuran (Fig. S20†). The analogous Ir(III) complex alone possesses absorption bands around 350–500 nm. Such a short absorption wavelength is not suitable for practical clinical applications.[63] The molar absorption coefficient at 650 nm follows the sequence **4-Ir** NPs ($\varepsilon = 10 \times 4.12$ M^{-1} cm^{-1}) > **1-Ir** NPs ($\varepsilon = 10 \times 3.84$ M^{-1} cm^{-1}) > **TPP** NPs ($\varepsilon = 10 \times 3.38$ M^{-1} cm^{-1}) consistent with efficient intramolecular energy transfer between the porphyrin and the Ir centers. The simulated absorption spectra for **TPP** and **4-Ir** in the long-wavelength region by TDDFT/B3LYP methods (Fig. S23†) also indicate that **4-Ir** NPs possess stronger absorption than that of **TPP** NPs at 550 nm. The NPs all exhibited NIR emission (Fig. 2D). The emission intensity of **TPP** NPs at 720 nm is 1.84 and 7.14 times higher than **1-Ir** NPs and **4-Ir** NPs, respectively. In addition, **L4** and **TPP** exhibit similar photophysical properties (Fig. S21†). The increased molar absorbance coefficient and the reduced emission intensity are conducive to accelerating the transfer of excited energy to the triplet state and to nonradiative vibrational processes, thereby improving the efficiency of both PDT and PTT.[64]

The photoluminescence quantum yields (PLQYs) in water of **TPP** NPs (29%) are higher than those of **1-Ir** NPs and **4-Ir** NPs (11% and 5%, respectively) (Table S2†). The fluorescent quantum efficiency and k_r values decrease from **TPP** NPs, **1-Ir** NPs to **4-Ir** NPs, while k_{nr} gradually increases from **TPP** NPs, **1-Ir** NPs to **4-Ir** NPs. **4-Ir** NPs are more likely to promote highly effective ISC which is beneficial to efficient utilization of the absorbed light energy for PDT and PTT. The excited-state lifetimes (τ) of **TPP** NPs (4.32 ns), **1-Ir** NPs (4.67 ns) and **4-Ir** NPs (4.82 ns) are all at the nanosecond level (Table S2†), meaning that the fluorescence of **1-Ir** NPs and **4-Ir** NPs is from the porphyrin unit and not from the phosphorescent Ir complexes. Meanwhile, the τ values gradually increase in the order **TPP** NPs< **1-Ir** NPs < **4-Ir** NPs, which is more conducive to the generation of a long-lived triplet photoexcited state from **4-Ir** NPs. This favors the full energy transfer between **4-Ir** NPs and oxygen molecules in the process of photodynamic therapy to obtain high-efficiency singlet oxygen. Together with the computational results, these experimental data demonstrate that **4-Ir** NPs fully achieve our molecular design objective of iridium-porphyrin conjugate nanoparticles with long wavelength excitation and near-infrared emission for synergistic PDT and PTT treatment.

High $^1O_2$ generation is a pre-requisite for efficient PDT.[65,66] The $^1O_2$ generation ability of **TPP** NPs, **1-Ir** NPs and **4-Ir** NPs was monitored by using 1,3-diphenylisobenzofuran (DPBF) as an indicator. Negligible spectral changes were observed in the control groups: (i) DPBF + irradiation (635 nm, 0.4 W cm^{-2}, 90 s); (ii) PSs + irradiation; and (iii) DPBF + PSs, indicating excellent photostability. As expected, upon irradiation, a continuous and significant decrease of absorbance was observed for solutions of PSs and DPBF consistent with efficient $^1O_2$ generation (Fig. 2E and S23†). In contrast, the absorption spectra were essentially unchanged with time for the following samples: (i) DPBF + NPs (Fig. S25†); (ii) NPs + irradiation (Fig. S26†) and (iii) DPBF + irradiation (Fig. S28†). The $^1O_2$ generation of all the PSs follows first-order kinetics (Fig. 2F). The slopes are in the order of **TPP** NPs (0.00637) < **1-Ir** NPs (0.01859) < **4-Ir** NPs (0.02654). Notably, the slopes of **1-Ir** NPs and **4-Ir NPs** are 2.92 and 4.17

times higher than that of **TPP** NPs, respectively. The $^1O_2$ quantum yields of **TPP** NPs, **1-Ir** NPs and **4-Ir** NPs are 54%, 72% and 89%, respectively, with methylene blue (MB) as the reference ($\Phi\Delta = 52\%$ in MeCN). These results confirmed that the **4-Ir** NPs exhibit the highest $^1O_2$ generation ability.

Subsequently, the photothermal activity of the NPs was evaluated. Upon laser irradiation (635 nm, 0.8 W cm^{-2}, 300 s), the aqueous solution temperatures of **TPP** NPs, **1-Ir** NPs and **4-Ir** NPs (6×10^{-5} M) increased from room temperature to 43.3, 46.9 and 59.1 °C, respectively, demonstrating photothermal activity (Fig. 3A). In addition, the solution temperature of **4-Ir** NPs increased with the increasing concentration and the laser power density (Fig. 3B and C). The photothermal conversion efficiencies (η) of **TPP** NPs, **1-Ir** NPs and **4-Ir** NPs are 31.2%, 37.8% and 49.5%, respectively (Fig. S29†). These data clearly indicate that the Ir centers significantly improve the photothermal effect. The data for **4-Ir** NPs are shown in Fig. 3D–F, including five heating-cooling cycles which verify excellent photothermal stability. The thermal images of **TPP** NPs, **1-Ir** NPs and **4-Ir** NPs were observed upon 635 nm laser irradiation for 10 min; the temperature of **4-Ir** NPs (71.5 °C) is higher than that of **1-Ir** NPs (60.3 °C) and **TPP** NPs (47.4 °C) (Fig. S30†). Furthermore, both the absorbance and PL intensity of **4-Ir** NPs retain more than 90% of their initial values after irradiation with a 635 nm laser (0.8 W cm^{-2}, 5 min) for 7 days (Fig. S31†). These results confirm that PSs based on a TPP-Ir(III) system display prominent photothermal effects and excellent optical stability.

The phototherapeutic efficacy of **TPP** NPs, **1-Ir** NPs and **4-Ir** NPs was determined against HeLa cells by using a 3-(4,5-dimethylthiazol-2-yl)-2,5-diphenyltetrazolium bromide (MTT) assay. In the dark, the cell viability exceeded 95% after incubation with **TPP** NPs, **1-Ir** NPs and **4-Ir** NPs, revealing good cytocompatibility (Fig. 4A). In contrast, under laser irradiation

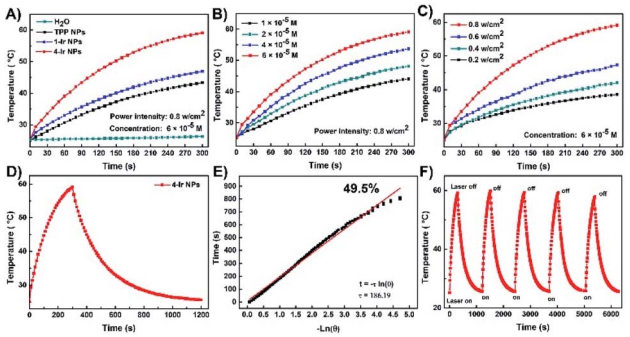

Fig. 3 (A) Photothermal heating curves of water, **TPP** NPs, **1-Ir** NPs and **4-Ir** NPs (6×10^{-5} M) in aqueous solution under irradiation (635 nm, 0.8 W cm^{-2}); (B) **4-Ir** NPs with different concentrations under irradiation (635 nm, 0.8 W cm^{-2}); (C) **4-Ir** NPs (6×10^{-5} M) with different laser power densities; (D) photothermal effect of the **4-Ir** NPs (6×10^{-5} M) dispersions under irradiation (635 nm, 0.8 W cm^{-2}), which was turned off after irradiation for 300 s; (E) plot of cooling time *versus* negative natural logarithm of the temperature obtained from the cooling stage of the **4-Ir** NPs; (F) temperature variations of the **4-Ir** NPs under irradiation (635 nm, 0.8 W cm^{-2}) for five light on/off cycles (300 s of irradiation for each cycle).

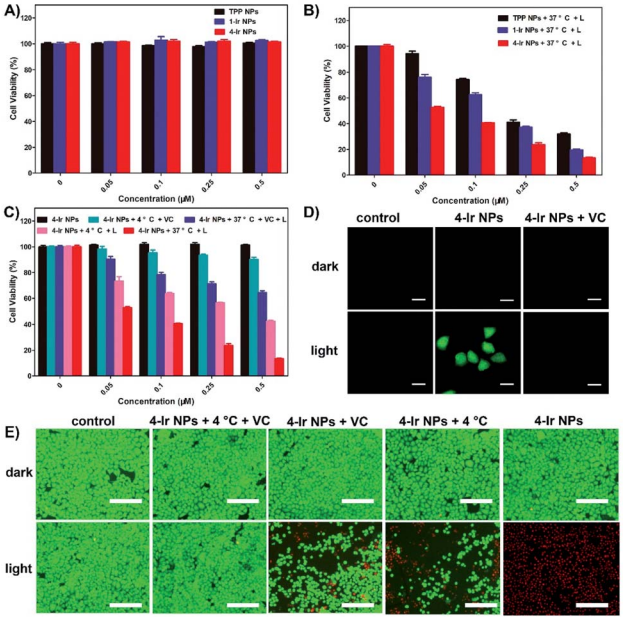

Fig. 4 Cell viability of different PSs against HeLa cells. (A) in the dark and (B) under light (L) (635 nm, 0.6 W cm^{-2}, 5 min); (C) cell viability of **4-Ir** NPs against HeLa cells under different conditions; VC = Vitamin C; (D) generation of intracellular reactive oxygen species (ROS) mediated by **4-Ir** NPs (0.5 μM) upon irradiation (635 nm, 0.6 W cm^{-2}, 3 min) as indicated by the fluorescence of DCFH-DA, the scale bars are 20 μm; (E) fluorescence images of live cells (green) and dead cells (red) with **4-Ir** NPs (0.5 μM) under irradiation (635 nm, 0.6 W cm^{-2}, 5 min), the scale bars are 40 μm.

(635 nm, 0.6 W cm^{-2}, 5 min), **TPP** NPs, **1-Ir** NPs and **4-Ir** NPs showed a concentration-dependent cytotoxicity (Fig. 4B). The order of the half-maximal inhibitory concentration (IC_{50}) is as follows: **TPP** NPs (0.225 μM) > **1-Ir** NPs (0.145 μM) > **4-Ir** NPs (0.057 μM). The lower IC_{50} value with **4-Ir** NPs validates that more Ir centers can enhance the therapeutic effect. A similar effect was observed in HeLa cells after incubation with **4-Ir** NPs for 72 h (Fig. S32†). Furthermore, the inhibition rate slightly reduced with 62.2% in the presence of Vitamin C, while the viability of cells decreased with 42.1% treated with a temperature of 4 °C (Fig. 4C). These results indicated that **4-Ir** NPs possess synergetic PDT and PTT effects, and that the PDT effect is dominant.

The intracellular ROS generation has also been investigated by using 2′,7′-dichlorofluorescin diacetate (DCFH-DA) as a probe (Fig. 4D). Negligible green fluorescence was detected in the control groups indicating a lack of ROS generation: (i) DCFH-DA only (control); (ii) DCFH-DA + **4-Ir** NPs; (iii) DCFH-DA + **4-Ir** NPs + Vitamin C; (iv) DCFH-DA + irradiation. However, obvious green fluorescence was monitored from the cells cultured with **4-Ir** NPs containing DCFH-DA under irradiation, whereas green fluorescence disappeared when the ROS capturer Vitamin C was added, indicating the effective generation of ROS in the cells. (Fig. S23†). Besides, bright field images show that the cells remain alive (Fig. S35†). The live/dead staining experiments further visually investigated the therapeutic effect of **4-Ir** NPs *in vitro* (Fig. 4E). Upon laser irradiation, negligible green

fluorescence was observed, implying that almost all of the cells were killed by **4-Ir** NPs. In contrast, under the same conditions, significant green fluorescence was monitored from the cells treated at 4 °C and with Vitamin C. Compared with the 4 °C treatment, the cells with Vitamin C exhibited brighter green fluorescence, proving the inhibition rate evidently decreased. These results are in accordance with the MTT assay.

The intracellular uptake and distribution of **TPP** NPs, **1-Ir** NPs and **4-Ir** NPs were evaluated in HeLa cells. Confocal laser scanning microscopy (CLSM) showed that all the NPs exhibited comparable intracellular red emission, suggesting that they can be internalized by living cells (Fig. S33†). In addition, the relatively weak red fluorescence observed in HeLa cells treated with sodium azide which causes energy depletion (Fig. S34†) suggests that energy-mediated endocytosis is the primary uptake pathway for the NPs. These results convincingly verify the excellent biocompatibility and outstanding synergistic PDT and PTT treatment effect of **4-Ir** NPs.

Inspired by the *in vitro* performance, **4-Ir** NPs were assessed *in vivo* with U14 tumor-bearing mice. These murine models were randomized into six groups: (1) with saline; (2) with saline + light; (3) **4-Ir** NPs + IT; (4) **4-Ir** NPs + IV; (5) **4-Ir** NPs + IT + light, (6) **4-Ir** NPs + IV + light. As shown in Fig. S36,† the strong fluorescence intensity of U14 tumor-bearing mice after intravenous (IV) injection with IR780-labeled **4-Ir** NPs into the tumor gradually increased within 12 h (with negligible residues in surrounding tissues) showing rapid and high accumulation of **4-Ir** NPs. These data indicated that 12 h after injection is the optimal time for light irradiation. An infrared thermal camera was used to monitor the temperature changes at the tumor sites. As illustrated in Fig. 5A and C, the temperature reached a plateau of 61.9 °C and 53.0 °C with intratumoral (IT) and intravenous injection after 10 min irradiation, respectively, manifesting the superior photothermal imaging and treatment effect. The tumor volume increased swiftly during two weeks in groups 1 to 4 (Fig. 5D), demonstrating that neither laser irradiation alone, nor **4-Ir** NPs alone, could suppress tumor growth. In sharp contrast, markedly reduced tumor volume and weight was observed in both groups 5 and 6 (Fig. 5B and F), indicating the outstanding tumor inhibition efficiency of **4-Ir** NPs under irradiation. The white spot in Fig. 5B indicates that the tumor tissue had been completely killed. For the tumors in groups 5 and 6, **4-Ir** NPs had a highly efficient tumor inhibition rate exceeding 90% (Fig. S37†). This can be attributed to the enhanced permeability and retention (EPR) effect of **4-Ir** NPs for systematically enhanced tumor targeting. There was no abnormal murine body weight loss in groups 2 to 6 (Fig. 5E), validating the minimal systemic toxicity of **4-Ir** NPs.

To study further the biodistribution of **4-Ir** NPs, the *ex vivo* fluorescence images of the major organs and tumor were obtained (Fig. S38 and S39†). The strongest fluorescence intensity was observed from tumor, liver and kidney. H&E-stained images of heart, liver, spleen, lung, kidney and tumor from sacrificed mice in each group were collected and assessed. No noticeable abnormalities in major organs from the six treatment groups were discovered, implying that **4-Ir** NPs are harmless *in vivo*. However, the tumor slices from groups 5 and 6 exhibit obvious

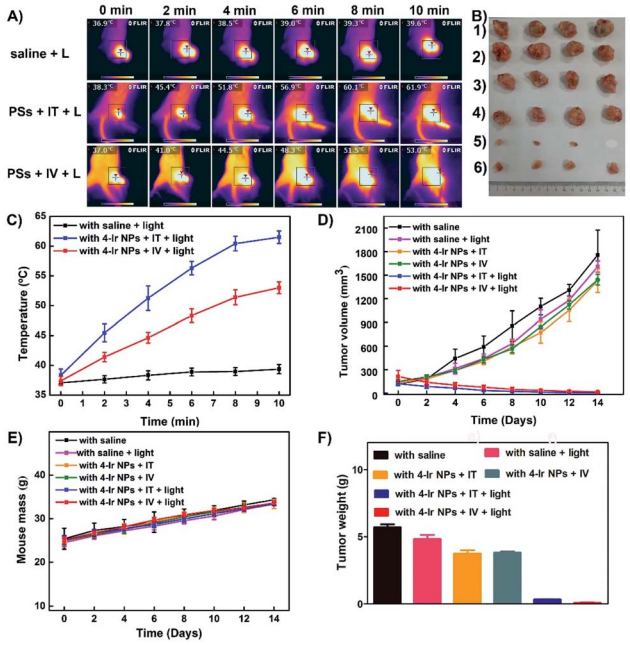

Fig. 5 (A) Photothermal imaging of mice treated with **4-Ir** NPs (100 μg mL^{-1}, 100 μL) under 635 nm laser irradiation at intensity 360 J cm^{-2} for 10 min; (B) harvested tumors from various groups of mice after treatment; (C) temperature of tumors monitored by the infrared thermal camera in different groups upon laser irradiation; (D) tumor volume measurement for different groups of mice; (E) body weights for different groups of mice; (F) tumor weights of six groups, representing the total weight of four samples in each group.

cellular nuclei damage, suggesting that **4-Ir** NPs caused cell apoptosis and necrosis. All these results indicated that **4-Ir** NPs are eminently suitable for phototherapy *in vivo*.

Conclusions

In summary, this work has demonstrated that iridium–porphyrin conjugates encapsulated in nanoparticles can act as PSs for photothermal imaging-guided synergistic PDT and PTT therapy. Two deep-red absorbing, NIR-emitting compounds were rationally designed and synthesized. The small ΔE_{ST}, separation of HOMO–LUMO, abundant and effective photoexcited state and high spin–orbit coupling constant increases with the number of peripheral Ir centers, thereby increasing the molar absorption coefficient at long wavelengths (635 nm), $^1O_2$ production capacity and photothermal activity. Especially, **4-Ir** NPs are ideal PSs for cancer treatment because of the following advantages: deep-red absorption, long-wavelength excitation (635 nm), NIR emission, remarkable $^1O_2$ generation ability, excellent photothermal conversion efficiency (49.5%), negligible dark toxicity and low IC_{50} (0.057 μM). Furthermore, both intravenous and intratumoral injections of **4-Ir** NPs exhibited an obvious temperature rise and high-efficiency inhibitory effect for tumor growth *in vivo*. This study provides new insights in the design of multifunctional PSs with long excitation wavelength for clinical therapeutic applications.

Author contributions

L. Z., Z. X. and D. Z. designed the experiments and the research. Y. G., L. Z., L. L., X. T., S. L. and X. L. performed the experiments. L.Z., Z. S., Z. X. and D. Z. analyzed the data. L. Z., Z. X., D. Z. and M. R. B. wrote the paper. All authors discussed the results and commented on the manuscript.

Conflicts of interest

There are no conflicts to declare.

Acknowledgements

All animal studies were performed in strict accordance with the NIH guidelines for the care and use of laboratory animals (NIH Publication No. 85-23 Rev. 1985) and were approved by the guidelines of the Committee on Animal Use and Care of the Chinese Academy of Sciences. The work was funded by NSFC (No. 52073045), the key scientific and technological project of Jilin province (20190701010 GH), the Development and Reform Commission of Jilin province (2020C035-5). D. X. Zhu thanks the support from Key Laboratory of Nanobiosensing and Nanobioanalysis at Universities of Jilin Province. M. R. B. thanks EPSRC grant EL/L02621X/1 for funding. The authors acknowledge the support from Jilin Provincial Department of Education.

Notes and references

1 E. J. Anthony, E. M. Bolitho, H. E. Bridgewater, O. W. L. Carter, J. M. Donnelly, C. Imberti, E. C. Lant, F. Lermyte, R. J. Needham, M. Palau, P. J. Sadler, H. Shi, F. Wang, W. Zhang and Z. Zhang, *Chem. Sci.*, 2020, **11**, 12888–12917.

2 H. Huang, S. Banerjee, K. Qiu, P. Zhang, O. Blacque, T. Malcomson, M. J. Paterson, G. J. Clarkson, M. Staniforth and V. G. Stavros, *Nat. Chem.*, 2019, **11**, 1041–1048.

3 R. Bevernaegie, B. Doix, E. Bastien, A. Diman, A. Decottignies, O. Feron and B. Elias, *J. Am. Chem. Soc.*, 2019, **141**, 18486–18491.

4 W. Lv, Z. Zhang, K. Y. Zhang, H. Yang, S. Liu, A. Xu, S. Guo, Q. Zhao and W. Huang, *Angew. Chem., Int. Ed.*, 2016, **55**, 9947–9951.

5 L. He, C. P. Tan, R. R. Ye, Y. Z. Zhao, Y. H. Liu, Q. Zhao, L. N. Ji and Z. W. Mao, *Angew. Chem., Int. Ed.*, 2014, **126**, 12333–12337.

6 H. Shi, X. Ma, Q. Zhao, B. Liu, Q. Qu, Z. An, Y. Zhao and W. Huang, *Adv. Funct. Mater.*, 2014, **24**, 4823–4830.

7 J. J. Conesa, A. C. Carrasco, V. Rodríguez-Fanjul, Y. Yang, J. L. Carrascosa, P. Cloetens, E. Pereiro and A. M. Pizarro, *Angew. Chem., Int. Ed.*, 2020, **59**, 1270–1278.

8 C. Jin, F. Liang, J. Wang, L. Wang, J. Liu, X. Liao, T. W. Rees, B. Yuan, H. Wang, Y. Shen, Z. Pei, L. Ji and H. Chao, *Angew. Chem., Int. Ed.*, 2020, **59**, 15987–15991.

9 J. S. Nam, M. Kang, J. Kang, S. Park, S. J. C. Lee, H. Kim, J. K. Seo, O. Kwon, M. H. Lim, H. Rhee and T. Kwon, *J. Am. Chem. Soc.*, 2016, **138**, 10968–10977.

10 S. M. King, S. Claire, R. I. Teixeira, A. N. Dosumu, A. J. Carrod, H. Dehghani, M. J. Hannon, A. D. Ward, R. Bicknell, S. W. Botchway, N. J. Hodges and Z. Pikramenou, *J. Am. Chem. Soc.*, 2018, **140**, 10242–10249.

11 J. Karges, S. Kuang, F. Maschietto, O. Blacque, I. Ciofini, H. Chao and G. Gasser, *Nat. Commun.*, 2020, **11**, 3262.

12 P. Wang, S. Guo, H. Wang, K. Chen, N. Zhang, Z. Zhang and T. Lu, *Nat. Commun.*, 2019, **10**, 3155.

13 V. Novohradsky, A. Rovira, C. Hally, A. Galindo, G. Vigueras, A. Gandioso, M. Svitelova, R. Bresolí-Obach, H. Kostrhunova, L. Markova, J. Kasparkova, S. Nonell, J. Ruiz, V. Brabec and V. Marchán, *Angew. Chem., Int. Ed.*, 2019, **58**, 6311–6315.

14 X. Li, J. Wu, L. Wang, C. He, L. Chen, Y. Jiao and C. Duan, *Angew. Chem., Int. Ed.*, 2020, **59**, 6420–6427.

15 R. Guan, Y. Chen, L. Zeng, T. W. Rees, C. Jin, J. Huang, Z. Chen, L. Ji and H. Chao, *Chem. Sci.*, 2018, **9**, 5183–5190.

16 X. Zheng, H. Tang, C. Xie, J. Zhang, W. Wu and X. Jiang, *Angew. Chem., Int. Ed.*, 2015, **54**, 8212–8217.

17 S. Kuang, X. Liao, X. Zhang, T. W. Rees, R. Guan, K. Xiong, Y. Chen, L. Ji and H. Chao, *Angew. Chem., Int. Ed.*, 2020, **59**, 3315–3321.

18 J. Zhao, K. Yan, G. Xu, X. Liu, Q. Zhao, C. Xu and S. Gou, *Adv. Funct. Mater.*, 2020, 2008325, DOI: 10.1002/adfm.202008325.

19 Z. Dong, L. Feng, Y. Hao, M. Chen, M. Gao, Y. Chao, H. Zhao, W. Zhu, J. Liu, C. Liang, Q. Zhang and Z. Liu, *J. Am. Chem. Soc.*, 2018, **140**, 2165–2178.

20 H. Min, J. Wang, Y. Qi, Y. Zhang, X. Han, Y. Xu, J. Xu, Y. Li, L. Chen, K. Cheng, G. Liu, N. Yang, Y. Li and G. Nie, *Adv. Mater.*, 2019, **31**, 1808200.

21 E. Palao, R. Sola-Llano, A. Tabero, H. Manzano, A. R. Agarrabeitia, A. Villanueva, I. López-Arbeloa, V. Martínez-Martínez and M. J. Ortiz, *Chem.–Eur. J.*, 2017, **23**, 10139–10147.

22 X. Zhang, Y. Hou, X. Xiao, X. Chen, M. Hu, X. Geng, Z. Wang and J. Zhao, *Coord. Chem. Rev.*, 2020, **417**, 213371.

23 V. Novohradsky, A. Rovira, C. Hally, A. Galindo, G. Vigueras, A. Gandioso, M. Svitelova, R. Bresolí-Obach, H. Kostrhunova, L. Markova, J. Kasparkova, S. Nonell, J. Ruiz, V. Brabec and V. Marchán, *Angew. Chem., Int. Ed.*, 2019, **58**, 6311–6315.

24 M. H. Chen, Y. Zheng, X. J. Cai, H. Zhang, F. X. Wang, C. P. Tan, W. H. Chen, L. N. Ji and Z. W. Mao, *Chem. Sci.*, 2019, **10**, 3315–3323.

25 Y. Liu, H. Wang, S. Li, C. Chen, L. Xu, P. Huang, F. Liu, Y. Su, M. Qi, C. Yu and Y. Zhou, *Nat. Commun.*, 2020, **11**, 1724.

26 Z. Zhang, W. Xu, M. Kang, H. Wen, H. Guo, P. Zhang, L. Xi, K. Li, L. Wang, D. Wang and B. Z. Tang, *Adv. Mater.*, 2020, **32**, 2003210.

27 S. B. Wang, C. Zhang, Z. X. Chen, J. J. Ye, S. Y. Peng, L. Rong, C. J. Liu and X. Z. Zhang, *ACS Nano*, 2019, **13**, 5523–5532.

28 W. Wang, L. Wang, Y. Li, S. Liu, Z. Xie and X. Jing, *Adv. Mater.*, 2016, **28**, 9320–9325.

29 Y. Yang, X. Fan, L. Li, Y. Yang, A. Nuernisha, D. Xue, C. He, J. Qian, Q. Hu, H. Chen, J. Liu and W. Huang, *ACS Nano*, 2020, **14**, 2509–2521.

30 Q. W. Chen, X. H. Liu, J. X. Fan, S. Y. Peng, J. W. Wang, X. N. Wang, C. Zhang, C. J. Liu and X. Z. Zhang, *Adv. Funct. Mater.*, 2020, **30**, 1909806.
31 K. Zhang, X. Meng, Y. Cao, Z. Yang, H. Dong, Y. Zhang, H. Lu, Z. Shi and X. Zhang, *Adv. Funct. Mater.*, 2018, **28**, 1804634.
32 Z. He, L. Zhao, Q. Zhang, M. Chang, C. Li, H. Zhang, Y. Lu and Y. Chen, *Adv. Funct. Mater.*, 2020, **30**, 1910301.
33 C. Yang, Y. Chen, W. Guo, Y. Gao, C. Song, Q. Zhang, N. Zheng, X. Han and C. Guo, *Adv. Funct. Mater.*, 2018, **28**, 1706827.
34 Q. Wan, R. Zhang, Z. Zhuang, Y. Li, Y. Huang, Z. Wang, W. Zhang, J. Hou and B. Z. Tang, *Adv. Funct. Mater.*, 2020, **30**, 2002057.
35 Y. Wang, N. Gong, Y. Li, Q. Lu, X. Wang and J. Li, *J. Am. Chem. Soc.*, 2020, **142**, 1735–1739.
36 W. Li, J. Yang, L. Luo, M. Jiang, B. Qin, H. Yin, C. Zhu, X. Yuan, J. Zhang, Z. Luo, Y. Du, Q. Li, Y. Lou, Y. Qiu and J. You, *Nat. Commun.*, 2019, **10**, 3349.
37 E. S. Shibu, M. Hamada, N. Murase and V. Biju, *J. Photochem. Photobiol., C*, 2013, **15**, 53–72.
38 Z. Yang, Z. Sun, Y. Ren, X. Chen, W. Zhang, X. Zhu, Z. Mao, J. Shen and S. Nie, *Mol. Med. Rep.*, 2019, **20**, 5–15.
39 M. Rizwan, T. Rasheed, A. Raza, M. Bilal, R. Yahya, M. Yar and H. M. N. Iqbal, *J. Drug Delivery Sci. Technol.*, 2019, **51**, 70–82.
40 J. Oh, H. Yoon and J. H. Park, *Biomed. Eng. Lett.*, 2013, **3**, 67–73.
41 R. D. Arasasingham and T. C. Bruice, *Inorg. Chem.*, 1990, **29**, 1422–1427.
42 H. S. Jung, P. Verwilst, A. Sharma, J. Shin, J. L. Sessler and J. S. Kim, *Chem. Soc. Rev.*, 2018, **47**, 2280–2297.
43 X. Zheng, L. Wang, S. Liu, W. Zhang, F. Liu and Z. Xie, *Adv. Funct. Mater.*, 2018, **28**, 1706507.
44 Q. Pei, X. Hu, X. Zheng, S. Liu, Y. Li, X. Jing and Z. Xie, *ACS Nano*, 2018, **12**, 1630–1641.
45 M. Rajora, J. Lou and G. Zheng, *Chem. Soc. Rev.*, 2017, **46**, 6433–6469.
46 X. Zheng, L. Wang, Y. Guan, Q. Pei, J. Jiang and Z. Xie, *Biomaterials*, 2020, **235**, 119792.
47 X. Zheng, L. Wang, M. Liu, P. Lei, F. Liu and Z. Xie, *Chem. Mater.*, 2018, **30**, 6867–6876.
48 J. Jin, Y. Zhu, Z. Zhang and W. Zhang, *Angew. Chem., Int. Ed.*, 2018, **57**, 16354–16358.
49 W. Liu, Y. M. Wang, Y. H. Li, S. J. Cai, X. B. Yin, X. W. He and Y. K. Zhang, *Small*, 2017, **13**, 1603459.
50 W. Hou, J. W. Lou, J. Bu, E. Chang, L. Ding, M. Valic, H. H. Jeon, D. M. Charron, C. Coolens and D. Cui, *Angew. Chem., Int. Ed.*, 2019, **58**, 14974–14978.
51 L. Zhang, Y. Li, W. Che, D. Zhu, G. Li, Z. Xie, N. Song, S. Liu, B. Z. Tang and X. Liu, *Adv. Sci.*, 2019, **6**, 1802050.
52 I. Toubia, C. Nguyen, S. Diring, L. M. A. Ali, L. Larue, R. Aoun, C. Frochot, M. Gary-Bobo, M. Kobeissi and F. Odobel, *Inorg. Chem.*, 2019, **58**, 12395–12406.
53 G. Lan, K. Ni, Z. Xu, S. S. Veroneau, Y. Song and W. Lin, *J. Am. Chem. Soc.*, 2018, **140**, 5670–5673.
54 J. Jiang, D. Liu, Y. Zhao, F. Wu, K. Yang and K. Wang, *Appl. Organomet. Chem.*, 2018, **32**, e4468.
55 Q. Zhang, Q. Zhang, Z. Li, H. Liu and J. Liu, *Dyes Pigm.*, 2020, **173**, 107923.
56 D. L. Davies, K. Singh, S. Singh and B. Villa-Marcos, *Chem. Commun.*, 2013, **49**, 6546–6548.
57 L. Zhang, W. Che, Z. Yang, X. Liu, S. Liu, Z. Xie, D. Zhu, Z. Su, B. Z. Tang and M. R. Bryce, *Chem. Sci.*, 2020, **11**, 2369–2374.
58 J. Dai, Y. Li, Z. Long, R. Jiang, Z. Zhuang, Z. Wang, Z. Zhao, X. Lou, F. Xia and B. Z. Tang, *ACS Nano*, 2020, **14**, 854–866.
59 B. Guo, Z. Huang, Q. Shi, E. Middha, S. Xu, L. Li, M. Wu, J. Jiang, Q. Hu and Z. Fu, *Adv. Funct. Mater.*, 2020, **30**, 1907093.
60 J. Karges, U. Basu, O. Blacque, H. Chao and G. Gasser, *Angew. Chem., Int. Ed.*, 2019, **58**, 14334–14340.
61 P. Zhang, X. Nie, M. Gao, F. Zeng, A. Qin, S. Wu and B. Z. Tang, *Mater Chem Front*, 2017, **1**, 838–845.
62 G. Lin, P. N. Manghnani, D. Mao, C. Teh, Y. Li, Z. Zhao, B. Liu and B. Z. Tang, *Adv. Funct. Mater.*, 2017, **27**, 1701418.
63 Y. You, H. S. Huh, K. S. Kim, S. W. Lee, D. Kim and S. Y. Park, *Chem. Commun.*, 2008, 3998–4000.
64 M. H. Chen, Y. Zheng, X. J. Cai, H. Zhang, F. X. Wang, C. P. Tan, W. H. Chen, L. N. Ji and Z. W. Mao, *Chem. Sci.*, 2019, **10**, 3315–3323.
65 Y. Gao, X. Wang, X. He, Z. He, X. Yang, S. Tian, F. Meng, D. Ding, L. Luo and B. Z. Tang, *Adv. Funct. Mater.*, 2019, **29**, 1902673.
66 W. Sun, T. Shi, L. Luo, X. Chen, P. Lv, Y. Lv, Y. Zhuang, J. Zhu, G. Liu and X. Chen, *Adv. Mater.*, 2019, **31**, 1808024.